APPLIED PHYSICS

Dynamically controllable polarity modulation of $MoTe_2$ field-effect transistors through ultraviolet light and electrostatic activation

Enxiu Wu[1]*, Yuan Xie[1]*, Jing Zhang[1], Hao Zhang[1], Xiaodong Hu[1], Jing Liu[1†], Chongwu Zhou[2†], Daihua Zhang[1†]

Copyright © 2019 The Authors, some rights reserved; exclusive licensee American Association for the Advancement of Science. No claim to original U.S. Government Works. Distributed under a Creative Commons Attribution NonCommercial License 4.0 (CC BY-NC).

Energy band engineering is of fundamental importance in nanoelectronics. Compared to chemical approaches such as doping and surface functionalization, electrical and optical methods provide greater flexibility that enables continuous, reversible, and in situ band tuning on electronic devices of various kinds. In this report, we demonstrate highly effective band modulation of $MoTe_2$ field-effect transistors through the combination of electrostatic gating and ultraviolet light illumination. The scheme can achieve reversible doping modulation from deep n-type to deep p-type with ultrafast switching speed. The treatment also enables noticeable improvement in field-effect mobility by roughly 30 and 2 times for holes and electrons, respectively. The doping scheme also provides good spatial selectivity and allows the building of a photo diode on a single $MoTe_2$ flake with excellent photo detection and photovoltaic performances. The findings provide an effective and generic doping approach for a wide variety of 2D materials.

INTRODUCTION

Two-dimensional (2D) transition metal dichalcogenides (TMDs) have been considered as promising building blocks for next-generation nanoelectronic (*1*–*5*) and optoelectronic (*6*–*8*) devices. TMDs have atomic layers that are held together by van der Waals forces. The absence of interlayer covalent bonds makes TMDs excellent electronic transport channels with very few scattering centers. They also exhibit great chemical stability due to the lack of dangling bonds on the surface (*2*, *9*), making them promising candidate materials for a variety of electronic devices including complementary metal-oxide semiconductors (CMOSs) (*3*–*5*), tunneling field-effect transistors (TFETs) (*10*, *11*), and photo diodes (*12*–*15*). Unipolar p- and n-type FETs with controllable transport properties are building blocks of these devices and of fundamental importance to their implementation and operation. Two particular TMDs, MoS_2 and WSe_2, have received the most research interest in this context. Each material has its own pros and cons. Concretely, n-type MoS_2 FETs can commonly achieve large on-off ratio and high electron mobility (*4*), but the p-type transport is exceedingly difficult due to strong Fermi-level pinning at the metal-MoS_2 interface (*16*, *17*). In addition, the bandgap of MoS_2 (1.3 to 1.8 eV) is too large for a TFET to produce sufficient tunneling efficiency in most cases. On the other hand, WSe_2 has a similar bandgap but a lower electron affinity, which creates comparable Schottky barriers for electrons and holes (*18*, *19*) when interfacing with most metal electrodes. It can therefore function as both p- and n-type channels. However, both carriers need to overcome large energy barriers at the metal contacts, resulting in low field-effect mobility and on-state current density.

Recently, another material in the TMD family, $MoTe_2$, has received increasing attention due to its intriguing semiconducting, metallic, and superconducting properties (*20*–*25*). $MoTe_2$ has a direct bandgap of 0.88 to 1.1 eV depending on its lattice arrangement and thickness (*21*–*23*). It is considerably smaller compared to those of MoS_2 (*2*, *8*) and WSe_2 (*18*, *19*), making $MoTe_2$ an excellent candidate for optoelectronic devices working in the near-infrared wavelength range (*26*). The small bandgap also enables large tunneling current and high on-off ratio of $MoTe_2$-based TFETs. Fermi-level pinning at the $MoTe_2$-metal interface is much weaker compared to sulfur-terminated TMDs (*27*). This, combined with the small bandgap, allows highly effective band modulation and carrier polarity control through multiple approaches. Previous studies fell into the following three categories. The first approach uses local electrostatic gating and has successfully demonstrated a p-n junction by configuring adjacent regions of a $MoTe_2$ flake into opposite polarities (*28*, *29*). The method is very flexible but volatile. The device loses its configuration as soon as the gating biases are withdrawn. The second type of scheme involves atomic doping and surface modification through a variety of chemical and physical means (*30*–*32*). They make permanent changes to the material, but p-type and n-type doping require distinct treatments that are difficult to integrate into the same device. The third method exploits work function engineering of the metal electrodes. Previous works have managed to turn ambipolar $MoTe_2$ into unipolar p-type FETs using high work function metals such as platinum (*33*). However, unipolar n-type transport was extremely hard to achieve, likely due to the combination of Fermi-level pinning and limited selection of low work function metals. Ideally, for carrier concentration and polarity control in $MoTe_2$, we need an approach that can provide nonvolatility, reversibility, high spatial resolution, and large dynamic range at the same time. However, such a solution is still lacking for $MoTe_2$ and for 2D materials in general.

In this work, we proposed a new approach to meet the above challenges. The scheme was inspired by floating gate memories.

[1]State Key Laboratory of Precision Measurement Technology and Instruments, School of Precision Instruments and Opto-electronics Engineering, Tianjin University, No. 92 Weijin Road, Tianjin 300072, China. [2]Department of Electrical Engineering, University of Southern California, Los Angeles, CA 90089, USA.
*These authors contributed equally to this work.
†Corresponding author. Email: jingliu_1112@tju.edu.cn (J.L.); chongwuz@usc.edu (C.Z.); zhangdaihua@gmail.com (D.Z.)

Concretely, we first created a charge storage interface under the conduction channel. Charging and discharging this interface require both optical [ultraviolet (UV) light] and electrical (electrostatic gating) activations, which ensures good nonvolatility and reversibility at the same time. The approach also provides a very large dynamic range from deep n-type to p-type doping, with the carrier concentration reaching 4.54×10^{12} and 4.95×10^{12} cm^{-2} for electrons and holes, respectively. The switching between opposite carrier polarities can be completed within a few milliseconds. Both n- and p-doped states are highly stable in ambient air with negligible degradation within 6 weeks of continuous monitoring. Although a similar strategy has been used in a graphene/boron nitride (BN) heterostructure, it fails to achieve unipolar n- or p-type doping in graphene (*34*). We have also observed a large improvement in field-effect mobility due to reduction of Schottky barriers at the $MoTe_2$-metal interface. Compared to pristine $MoTe_2$ FETs, the electrically doped n-type and p-type devices showed an increase in field-effect mobility by 2 and 30 times.

RESULTS AND DISCUSSION

Device architecture and electrical properties

Figure 1A shows the structural configuration of the $MoTe_2$ devices used in our study. The right half of the structure is a standard $MoTe_2$ FET back-gated through the Si/SiO_2 substrate. On the left half, we placed a thin layer of h-BN under the $MoTe_2$ flake, which creates two interfaces on the top and bottom surfaces of the BN. As will be discussed in the following sections, the BN/SiO_2 interface can effectively trap charges and fundamentally change the transport behaviors of the $MoTe_2$ FET. The half-half arrangement sets up a good control experiment for us to examine and compare the two configurations in parallel. Figure 1B presents a false-colored scanning electron microscopy (SEM) image of the structure. The two pairs of Cr/Au electrodes (labeled as 1/2 and 3/4) define a separate transport channel in each section. For convenience, we name the upper-right device (a standard $MoTe_2$ FET) and the lower-left one (with BN cushion layer) as device A and device B, respectively. The transport channel between electrodes 2 and 3 constitutes a

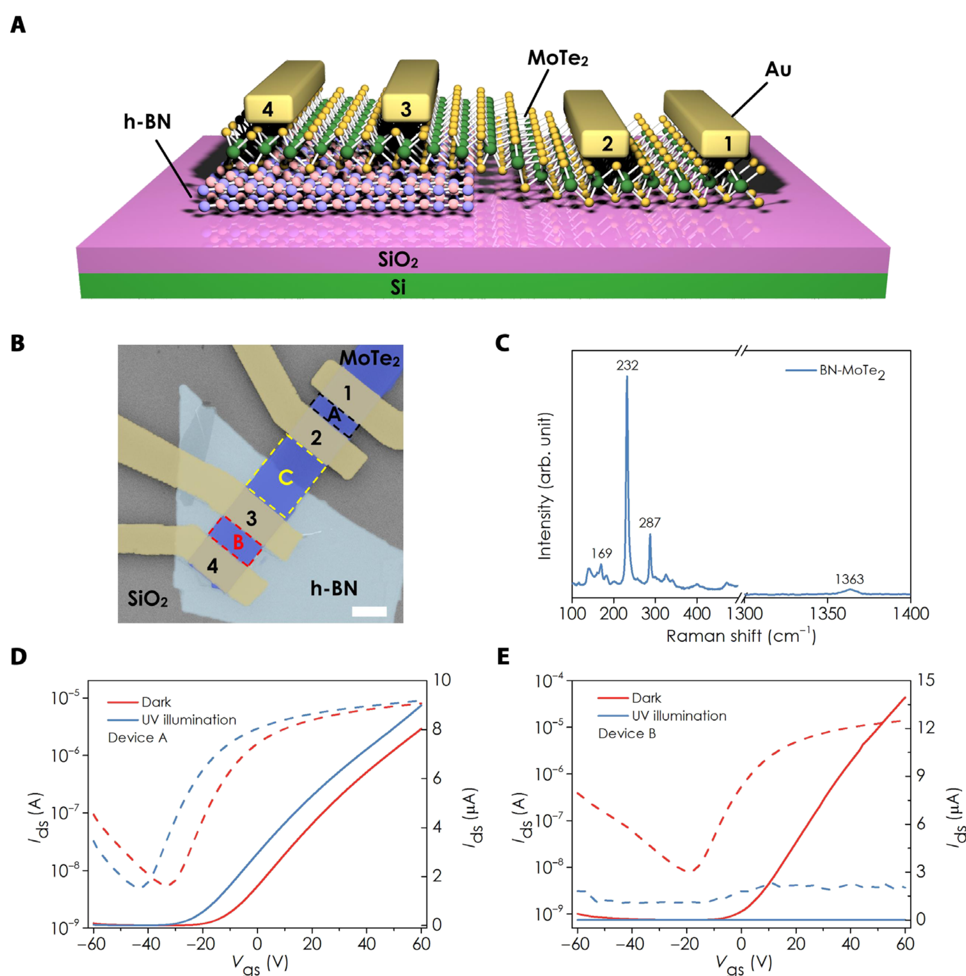

Fig. 1. Device architecture and electrical properties. (**A**) Schematic of a junction device used in the study. The $MoTe_2$ flake is a configurable semiconducting channel. The Si/SiO_2 substrate serves as a back gate. Under the left half of the $MoTe_2$ flake, we inserted a BN layer to create a BN/SiO_2 interface. (**B**) False-colored SEM image of the device. The light blue and dark blue regions are the sections with and without the BN "cushion" layer. The black and red dashed rectangles mark the transport channels defined by two pairs of metal electrodes, named device A and device B, respectively. The junction region between electrodes 2 and 3 is highlighted by the yellow dashed rectangle and named device C. Scale bar, 5 μm. (**C**) Raman spectrum of a $MoTe_2$/BN bilayer sample. Transfer characteristics of device A (**D**) and device B (**E**) in both linear (solid line) and semi-log (dashed line) scales. The V_{ds} was 500 mV. Despite similar characteristics in a dark environment, the two devices demonstrated entirely different behaviors under UV illumination.

junction device, which is named device C and will be discussed later in the last section. The Raman spectrum in Fig. 1C confirms the lattice structures of the $MoTe_2$ and h-BN nanocrystals. The three peaks at 169, 232, and 287 cm^{-1} are characteristic peaks of $MoTe_2$, and the peak at 1363 cm^{-1} originates from longitudinal mode phonons in h-BN. Thicknesses of the $MoTe_2$ and BN flakes were measured to be 28 and 11.5 nm using atomic force microscopy (AFM) (fig. S1).

Figure 1D shows the transfer characteristics of device A recorded in the dark (red) and under continuous UV light illumination (blue). The gate-source bias (V_{gs}) was scanned from +60 to −60 V while the drain-source bias (V_{ds}) remained at +500 mV. The corresponding output curves are shown in fig. S2 (A and B). Device A has no BN layer under the $MoTe_2$ channel. It behaves similarly to other $MoTe_2$ FETs in previous reports and provides reference data to our study. The device is essentially an ambipolar transistor with a dominant n-branch. As shown in the semi-log plots of Fig. 1D, the on-state current of the n-branch at V_{gs} = +60 V was significantly higher than the hole current at V_{gs} = −60 V by two to three orders of magnitude. The minimum conduction point (MCP) was originally located around −30 V and shifted to −45 V under UV light. The response was attributed to desorption of oxygen and moisture molecules from the $MoTe_2$ surface. Similar behaviors have been observed in previous studies and in other TMD materials as well (*8*, *35*). To make a side-by-side comparison, we plot the transfer characteristics curve of device B in Fig. 1E (output characteristics shown in fig. S2, C and D). The curve recorded in the dark (red) is qualitatively similar to that of device A, but the on-state current is considerably larger by roughly 30%. As has been discussed in previous studies (*36*, *37*), BN can form a cleaner interface with 2D materials with less charge trapping and scattering states compared to the case of direct contact with SiO_2. On the other hand, the I_{ds}-V_{gs} curve under UV light (blue) was totally unexpected. In notable contrast to device A, device B stayed in the off-state throughout the entire voltage scan from −60 to +60 V. It appears that the electrostatic gating was completely screened. The UV light could somehow trigger the redistribution of electrostatic charges in the microstructure, establishing a new field to counteract the gate bias.

Reversible doping of a $MoTe_2$ transistor and doping mechanisms

The experiments in Fig. 2 provide more details about this effect. Unlike the measurement in Fig. 1E, this time, we separate the UV illumination and the V_{gs} scanning into two steps. We first expose device B to UV light under a fixed activation gate bias (referred to as "writing voltage" in the following discussion) for 1 s and then perform a full scan of V_{gs} after the light turns off. The results are shown in Fig. 2A. The solid and dashed lines are linear and semi-log plots, respectively. The annotation lists the writing voltage used during the UV exposure step. The curve taken after the illumination under zero writing voltage shows no difference from the dark measurement of Fig. 1E, indicating that the UV illumination itself does not induce lasting changes to the device. The illumination under a positive writing voltage, however, does make a permanent change that remains even after the light and writing voltage are both withdrawn. The magnitude of the change is qualitatively proportional to the writing voltage applied during the illumination step. As the writing voltage increases from 0 to +30 V, the MCP of the $MoTe_2$ FET shifts from −20 to +50.4 V progressively (fig. S3A), indicating the potential of the method to quantitatively control the doping level. At the same time, the device transforms from an n-dominant ambipolar transistor (red curve) to a highly doped p-type unipolar FET (black curve). The results suggest that the internal E-field induced by the dual activation of UV illumination and electrostatic gating is nonvolatile and able to electrically dope the $MoTe_2$ channel to sufficiently deep levels. Figure 2B quantifies the charge transport properties by plotting the hole concentration (n_h) at V_{gs} = −40 V and mobility as a function of writing voltage. The hole mobility (amber curve) jumps from 2.6 to 58.9 $cm^2\ V^{-1}\ s^{-1}$ at +20 V and keeps a constant level under higher activation biases. On the other hand, the electron mobility (red curve) decreases quickly to near zero as the device polarity transforms from n to p. The hole concentration, as shown by the blue curve, increases by one order of magnitude from 1.37×10^{11} to $4.95 \times 10^{12}\ cm^{-2}$ at the highest doping level.

The measurements in Fig. 2C demonstrate that the same scheme can also dope the device in the opposite way, from an ambipolar to a unipolar n-type FET. This time, we applied negative writing voltage during the UV exposure. The field-effect mobility and electron concentration (n_e) are plotted in Fig. 2D. The electron mobility and concentration increased markedly by two times (from 22.5 to 40.2 $cm^2\ V^{-1}\ s^{-1}$) and three times (from 1.46×10^{12} to $4.54 \times 10^{12}\ cm^{-2}$) after doping. In contrast, the hole mobility dropped from 2.87 to 0.0037 when the polarity switching took place. We note that the hole mobility in our p-type FET (58.8 $cm^2\ V^{-1}\ s^{-1}$) is so far the highest value achieved with $MoTe_2$. The electron mobility (40.2 $cm^2\ V^{-1}\ s^{-1}$) in the n-type device also outperforms most $MoTe_2$ FETs except the one reported in (*30*) using solution-based doping (*20*, *21*, *31*–*33*, *22*–*26*, *28*–*30*). The shift of MCP with writing voltage is plotted in fig. S3B. As writing voltage increases from −5 to −50 V, the position of MCP of the $MoTe_2$ FET linearly shifts from −13.2 to −52.8 V.

To verify the repeatability of the doping process, we have carried out the same measurements on four other devices. They all behaved very consistently in response to the dual activation of UV light and electrostatic gating (fig. S4). Besides, we have also observed qualitatively similar behaviors in WSe_2/BN and MoS_2/BN devices (fig. S5). A major difference is, however, that the MoS_2 device had a very small response to positive writing voltage under UV illumination (p-type doping) due to strong Fermi-level pinning at the metal-MoS_2 interface (*16*, *17*).

We then carried out a series of experiments to investigate the origin and mechanism of the photoinduced doping. First, we verified that the doping only occurred when the BN layer was present. Similar to device A, devices with their $MoTe_2$ channel in direct contact with the SiO_2 substrate showed absolutely no response to the optoelectrical activations (fig. S6). Second, we confirmed that the doping or polarity switching did not result from preadsorbed air molecules on the $MoTe_2$ surface. The experimental results of Fig. 2 (A to D) could be reliably reproduced in a N_2 environment after desorbing the air molecules (O_2 and H_2O) using UV light. Third, we found that the BN/SiO_2 interface is indispensable to enable p-type doping. In the experiment of Fig. 2E, we used Au as gate electrode to gate the $MoTe_2$ channel through the BN layer sandwiched in between. This way, we removed the BN/SiO_2 interface from the device while keeping its top structure the same. As shown in Fig. 2E, the optoelectrical activation only worked for n-type doping when negative writing voltage was applied during UV illumination. The device did not respond to positive writing voltage and therefore could not be p-type–doped. The results are consistent with the observation in (*34*), which reported on photoinduced n-type doping in

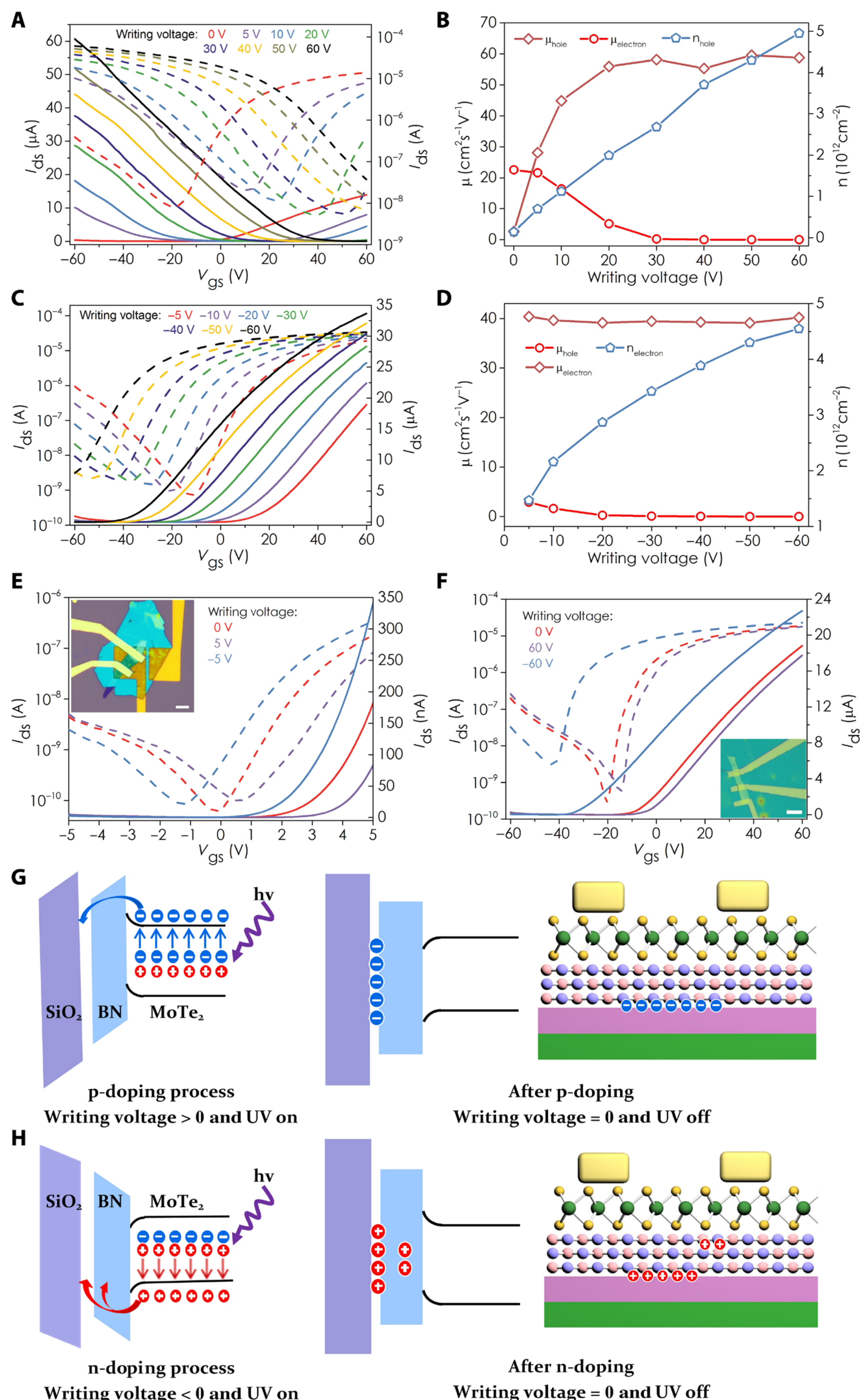

Fig. 2. Reversible doping of the $MoTe_2$transistor and doping mechanisms. (**A**) Transfer characteristic curves of device B at V_{ds} = 500 mV at different photoinduced p-type doping levels. Device B is exposed to UV illumination for 1 s at writing voltage = 5, 10, 20, 30, 40, 50, and 60 V. (**B**) Hole/electron mobility μ (left axis) and hole concentration (n_h) at V_{gs} = −40 V (right axis) from transfer characteristic traces in (A). (**C**) Transfer characteristic curves of device B at V_{ds} = 500 mV at different photoinduced n-type doping levels. Device B is exposed to UV illumination for 1 s at writing voltage = −5, −10, −20, −30, −40, −50, and −60 V. (**D**) Hole/electron mobility μ (left axis) and electron concentration (n_e) at V_{gs} = 40 V (right axis) from transfer characteristic traces in (C). (**E**) Transfer characteristics of the $MoTe_2$ transistor deposited with local gate after being exposed to UV illumination for 30 s at writing voltage = 5 and − 5 V. Inset: Optical image of the $MoTe_2$ transistor device with separated Au local gates; h-BN was the dielectric layer. (**F**) Transfer characteristics of the $MoTe_2$/BN heterostructure before and after photoinduced doping. The thickness of BN was 50 nm. Inset: Optical image of the device. (**G** and **H**) Left: Energy band diagrams of the device under p-type doping process (G)/n-type doping process (H). Right: Energy band diagrams and schematics of the device after p-type doping (G)/n-type doping (H). The red and blue circles represent the holes and electrons, respectively.

graphene/BN heterostructures by UV light. The report suggested that the doping arose from a series of microscopically coupled optical and electrical responses, including optical excitation of defect transitions in BN, electrical transport in graphene, and charge transfer between BN and graphene. However, the light illumination in (*34*) only activated n-type doping rather than both polarities. It appears that a BN layer is able to trigger electron doping by itself in the 2D material attached to it, but for p-type doping, a BN/SiO_2 interface is indispensable according to our experimental observations. Moreover, we measured the doping behaviors of the $MoTe_2$/BN heterostructure under the illumination of visible light with wavelengths of 400 and 500 nm, as shown in fig. S7. The device achieved much weaker p/n-type doping as compared to the doping level under UV illumination. It is also difficult to implement the polarity modulation of the device from n-type to p-type. The results indicate that light illumination with higher photon energy is easier to excite the BN/SiO_2 interface state and defect transitions in BN.

In light of the above experimental results, we propose the electrostatic p- and n-type doping energy band diagrams and schematics in Fig. 2 (G and H, respectively). The UV photons generate a large number of free electrons and holes in the $MoTe_2$ channel. For the p-type doping process, a positive writing voltage is applied in the vertical direction under UV illumination (Fig. 2G), which drives UV-excited electrons to tunnel through the BN layer. At the same time, the UV illumination also excites defect states at the BN/SiO_2 interface to trap and anchor these electrons. As a result, even after the optoelectrical activation is withdrawn, the electrons remain at the interface permanently, creating a negative gate bias to electrostatically dope the $MoTe_2$ channel, which shifts the Fermi level close to the valence band and decreases the Schottky barrier for hole transport, forming a p-type $MoTe_2$ transistor. Higher writing voltage results in larger tunneling current and higher density of electrons trapped in the BN/SiO_2 interface and therefore driving the device to deeper doping levels. For the n-type doping shown in Fig. 2H, holes can be trapped not only at the interface of BN/SiO_2 but also at the interface between BN/$MoTe_2$ and by the photoinduced defect states within the BN crystal, which create positive gating and electron doping in the $MoTe_2$ channel. The schematic of Fig. 2H manifests a slight difference between p- and n-type doping. This explains why n-type doping could still occur in the absence of the BN/SiO_2 interface. The data in Fig. 2F provide additional evidence in support of the proposed doping mechanism. In the experiment, we intentionally used a very thick BN (50 nm) in the device. The $MoTe_2$ FET showed detectable n-type doping driven by holes trapped within the BN layer. However, p-type doping was completely disabled as electrons could not tunnel through the thick BN and reach the interfacial states on the other end.

Fast doping of the $MoTe_2$ transistor and stability of the doped $MoTe_2$ device

Figure 3 examines the speed and stability of the photoinduced doping. We start with a highly doped p-type state, set V_{gs} to −60 V to turn on the device fully, and then monitor its drain-source current (I_{ds}) during UV illumination to record the dynamic process of its polarity switching. As shown in Fig. 3A, the steady I_{ds} was kept at 61.2 μA until UV light was turned on at 0.58 s. The current then dropped immediately to 5.52 nA, reaching the off-state of the n-type channel. The entire p-to-n transition took approximately 80 ms, as indicated in the figure. We then bias the n-type device to V_{gs} = +60 V to reach its on-state and then expose it to UV light and visualize its n-to-p transition process (Fig. 3B). The switching took ~600 ms this time, ~10 times slower than the n-to-p transition. The difference in transition speed is presumably due to different tunneling properties of electrons and holes as well as different densities and positions of their available trapping states. We note that the polarity switching is completely reversible and highly robust. By the time we finished this report, the device had undergone more than 300 cycles of switching without any detectable degradation. Figure 3 (C and D) evaluates the retention time of each state by repeatedly measuring its transfer characteristics over a 40-day time span. Both the n-state (Fig. 3C) and p-state (Fig. 3D) curves showed good repeatability over the entire monitoring. To better visualize the result, we plot the on-state current and threshold voltage (V_{th}) of each state as a function of time in the insets of Fig. 3 (C and D). Despite slight drifts in the first 5 to 10 days, values remained stable throughout the rest of the measurements.

Negligible hysteresis of the doped p/n-type $MoTe_2$ transistor

The results in Fig. 4 present another interesting feature of the doped $MoTe_2$ FET. The double scan of V_{gs} induces negligible hysteresis in the transfer curves of both the n-type (Fig. 4A) and p-type (Fig. 4C) states. This indicates that the I_{ds} is solely a function of V_{gs} and V_{ds}, independent of the device's previous history. This property is fundamentally important to all logic devices and electronic sensors. In Fig. 4 (B and D), we recorded the output characteristics of the n- and p-type states. Instead of monotonically increasing or decreasing the gate bias, we shuffled V_{gs} into random orders when taking these curves. The channel conductance derived from these linear curves is in perfect agreement with the I_{ds}-V_{gs} scans in Fig. 4 (A and C). We note that hysteresis in I_{ds}-V_{gs} curves commonly exists in most semiconducting nanomaterials (*36*, *38*). It is primarily caused by surface adsorptions and/or defect states that can trap charges during the V_{gs} scan. Highly doped devices are presumably more immune to these trapping states as dense dopants dominate the transport behaviors. On the contrary, chemical doping and plasma doping generally induce larger hysteresis due to introduction of more surface and defect states into the 2D materials. On the other hand, our optoelectrical doping scheme is based on pure electrostatic interactions that effectively minimize the I_{ds}-V_{gs} hysteresis. This provides an important and unique advantage over other doping methods.

Direct writing of a stable p-n junction and optoelectronic applications

The photoinduced doping scheme also provides good spatial selectivity, which would open up the possibility of a wide variety of functional devices including CMOSs, photo diodes, and TFETs. Selective doping can be implemented by the following three approaches. The first approach is to selectively expose local regions to UV light through a shadow mask or scanning laser, similar to the way laser printers are used to develop latent images on photo imaging plates. Alternatively, we can selectively apply electrostatic activations during UV illumination. This would, however, require local gate electrodes and introduce extra design and fabrication complexity. The third approach is to pattern the BN layer accordingly, leaving it only in the region that needs to be activated or doped. In the following section, we will use the third approach to create a $MoTe_2$ photo diode and evaluate its energy conversion and photo detection performances.

In fact, in the device shown in Fig. 1B, the conduction channel between electrodes 2 and 3 has already constituted a junction device

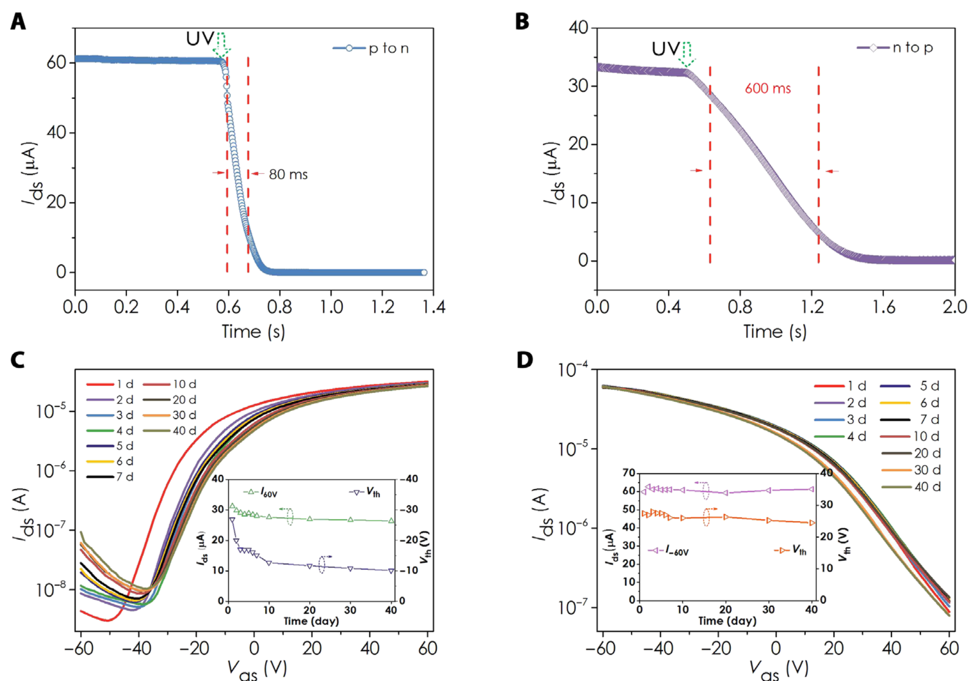

Fig. 3. Fast doping of the $MoTe_2$ transistor and stability of the doped $MoTe_2$ device. (**A**) p-to-n transition of device B. The device was biased at $V_{gs} = -60$ V throughout the measurement. UV light was turned on at ~0.58 s, switching the device from an on-state p-type FET to an off-state n-type FET within approximately 80 ms. (**B**) Switching process from on-state n-type FET to off-state p-type FET. The transition time is around 600 ms, ~10 times slower compared to the p-to-n transition. Stability tests of the doped n-type (**C**) and p-type (**D**) $MoTe_2$ FETs in ambient air and temperature. Insets are the on-state current and threshold voltage (V_{th}) of each state as a function of time. The V_{ds} was 500 mV.

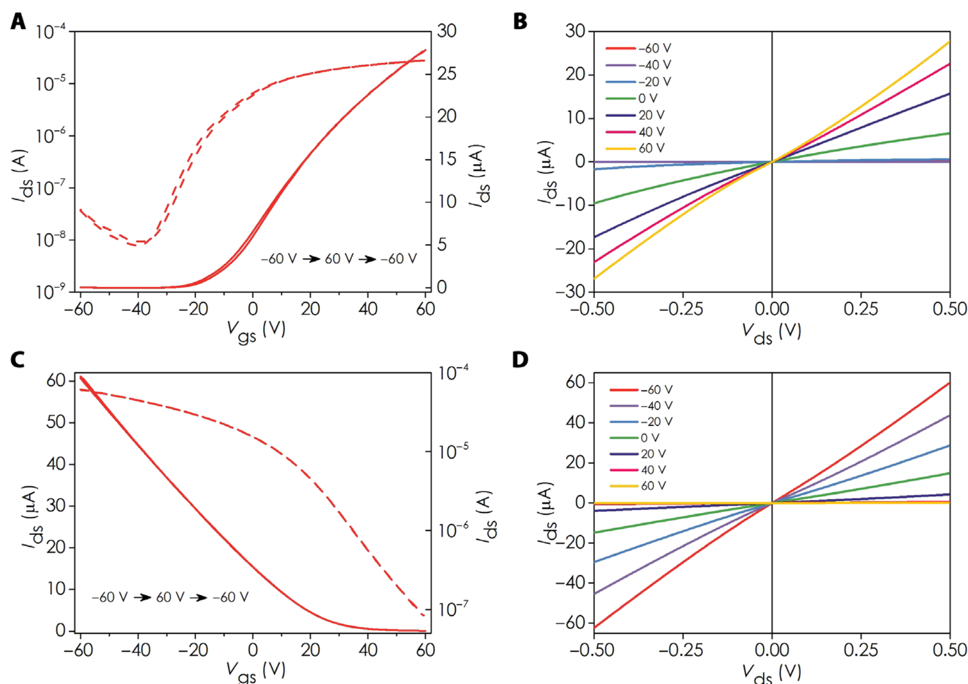

Fig. 4. Negligible hysteresis of the doped p/n-type $MoTe_2$ transistor. Transfer characteristic curves of device B at $V_{ds} = 500$ mV after intense n-type doping (**A**) and p-type doping (**C**). The sweeping directions were from −60 to +60 V in the positive direction and +60 to −60 V in the negative direction. The sweeping rate of V_{gs} was 1.2 V/s. Corresponding output characteristic curves at $V_{gs} = -60$, 60, −40, 40, −20, 20, and 0 V of the n-doped (**B**) and p-doped (**D**) $MoTe_2$ FETs.

(device C). The dark blue region is intrinsically n-doped (Fig. 1D), and the light blue region can be dynamically modulated through photoinduced doping. We can then dope this section to different p-levels and record the output characteristic of the junction device after each activation (Fig. 5A). The rectifying ratio increases monotonically with the doping level as the built-in potential across the p-n junction rises. The transfer characteristics in Fig. 5B show an unusual gate voltage dependence, which was referred to as "antiambipolar" behavior in previous studies (*39*, *40*). In particular, the conductance peaks around V_{gs} = 0 V in devices with highly doped p-sections, which is opposite to typical V-shape transfer characteristics of conventional ambipolar devices [like the ones in Fig. 2 (A to C)]. A simple way to understand this is to view the p-n junction as two FETs connected in series. It therefore contains two off-states, corresponding to the depletion of the p- and n-type FET, respectively. The channel conductance reaches its local maximum between these two off-states, creating a peak near V_{gs} = 0 V in the transfer characteristic curve.

The experiments in Fig. 5 (C and D) evaluate the photo response of the $MoTe_2$ p-n diode. We use a 550-nm (yellow) laser with a tunable output power of up to 1.25 nW. Figure 5C shows the output characteristics of device C under different illumination powers. The I_{ds}-V_{ds} curve shifts into the fourth quadrant gradually as the laser power increases. In this case, the p-n junction works as a photovoltaic device that reaches its highest output power of $P_{electrical} = 4.5 \times 10^{-3}$ nW at 30 mV and 150 pA. We estimated the incident optical power to be $P_{optical}$ = 1.25 nW according to the device area and power density of the illumination. The energy conversion efficiency is calculated to be $\eta_{PV} = P_{electrical}/P_{optical} \approx 0.36\%$, which is among the comparable values achieved by TMD-based photovoltaic devices (*14*, *41*, *42*), presumably due to highly effective doping of the $MoTe_2$ crystal. The fill factor, defined as the ratio between maximum obtainable power and the product of open-circuit voltage and short-circuit current, is calculated to be 0.25 at the highest illumination power of 1.25 nW.

The junction device also works as a photodetector under a fixed voltage bias. In Fig. 5D, we recorded the photo current at V_{ds} = 0 V during five consecutive illumination cycles. Curves in different colors were taken at different laser powers ranging from 0.18 to 1.25 nW. The device exhibits excellent sensitivity, repeatability, and stability. The photoresponsivity (R) reached 0.21 A/W as estimated at different incident powers. The external quantum efficiency (EQE) is proportional to R and defined as EQE = $hcR/e\lambda$, with h, c, e, and λ being the Planck constant, speed of light, elementary charge, and incident light wavelength, respectively. The EQE is calculated to be 47.7% in our case. We note that both the photoresponsivity and the EQE are considerable among all photo diodes built on a single piece of TMDs through selective doping (*42*–*46*). The photo detector also exhibits a very short response time of ~2 ms. Operating the device under non-zero bias can further shorten the response time to below 200 μs (fig. S8).

CONCLUSION

We developed a versatile optoelectrical doping approach that enables highly effective, nonvolatile, reversible, ultrafast, and spatially selective band modulation of $MoTe_2$ FETs. We also observed significant mobility and stability enhancement in both the n- and p-doped states. The scheme allowed us to build a p-n diode on a single piece of $MoTe_2$ flake, which demonstrated excellent photovoltaic and photo detection performances. Several performance specs reported in this

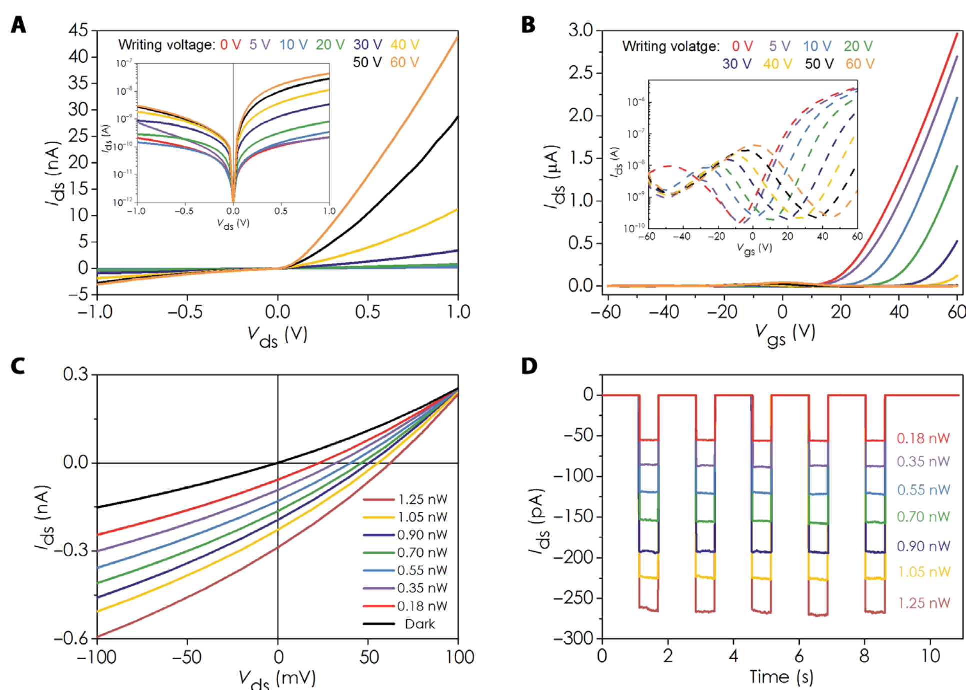

Fig. 5. Direct writing of a stable p-n junction and optoelectronic applications. (**A**) Output characteristic curves of device C at V_{gs} = 0 V after different photoinduced doping at writing voltage = 0, 5, 10, 20, 30, 40, 50, and 60 V. (**B**) Transfer characteristic curves of device C at V_{ds} = 500 mV after photoinduced modulation doping. (**C**) Output characteristic curves of the device under light illuminations of different powers. (**D**) Photo-switching characteristics of the device during multiple illumination cycles. V_{ds} = 0 V and V_{gs} = 0 V.

work, including hole and electron mobility, photoresponsivity, and EQE are among the highest values ever achieved by $MoTe_2$ and even all TMD materials. The doping approach paves a new way of band modulation in 2D materials and will likely enable a wide variety of device concepts and functions in electronic and optoelectronic applications.

MATERIALS AND METHODS

Device fabrication

The heterostructures were produced with a dry transfer technique. First, an h-BN flake was mechanically exfoliated from bulk h-BN and then transferred onto a 285-nm SiO_2/n+-doped Si substrate. Next, a $MoTe_2$ flake was transferred onto an h-BN flake to cover half of it. Last, electrodes were patterned by electron beam lithography with positive electron beam resist. Cr/Au (20/30 nm) was deposited by electron beam evaporation after exposure and development, which was followed by a standard liftoff process to complete the fabrication.

Electrical parameters calculation

The electron concentration (n_e) and hole concentration (n_h) of the $MoTe_2$ film can be extracted according to $n_{2D} = (I_{ds}L)/(qWV_{ds}\mu)$ at $V_{gs} = 40$ V and $V_{gs} = -40$ V, where q is the elementary charge and L and W are the channel length and width, respectively. μ is the field-effect mobility, which can be calculated using $\mu = G_m L/(V_{ds}C_{ox}W)$, where $G_m = dI_{ds}/dV_{gs}$ is the transconductance in the linear region of the transfer curve and $C_{ox} = 1.156 \times 10^{-8}$ F/cm^2 is the gate oxide capacitance.

Characterizations

We used a commercial Raman spectrometer (Renishaw Inc.) to obtain the Raman spectroscopy with a 532-nm laser source. The AFM images were taken with a Bruker Dimension Icon. The electrical properties were measured with an Agilent B1500A semiconductor parameter analyzer in ambient air. The wavelength and intensity of the used UV light were 254 nm and 2.5 mW/cm^2, respectively. The photovoltaic properties were characterized with a 550-nm laser, the power of which can be tuned continually. We used an optical power meter of PM100D to measure the power of the light and calculated the incident light power on the devices according to their area.

SUPPLEMENTARY MATERIALS

Supplementary material for this article is available at http://advances.sciencemag.org/cgi/content/full/5/5/eaav3430/DC1

Supplementary Materials and Methods

Fig. S1. AFM images of devices.

Fig. S2. Output characteristic curves of device A and device B.

Fig. S3. Position of MCP versus writing voltage in the p-type and n-type doping processes.

Fig. S4. Transfer characteristics of four other $MoTe_2$ samples under different doping conditions.

Fig. S5. Transfer characteristics of WSe_2 and MoS_2 under different doping conditions.

Fig. S6. Transfer characteristics of $MoTe_2$ on SiO_2 substrate under different conditions.

Fig. S7. Doping behaviors of the $MoTe_2$/BN device under visible light illumination.

Fig. S8. Dynamic response characteristics of device C at different V_{ds}.

REFERENCES AND NOTES

1. H. Liu, A. T. Neal, P. D. Ye, Channel length scaling of MoS_2 MOSFETs. *ACS Nano* **6**, 8563–8569 (2012).
2. B. Radisavljevic, A. Radenovic, J. Brivio, V. Giacometti, A. Kis, Single-layer MoS_2 transistors. *Nat. Nanotechnol.* **6**, 147–150 (2011).
3. H. Wang, L. Yu, Y.-H. Lee, Y. Shi, A. Hsu, M. L. Chin, L.-J. Li, M. Dubey, J. Kong, T. Palacios, Integrated circuits based on bilayer MoS_2 transistors. *Nano Lett.* **12**, 4674–4680 (2012).
4. B. Radisavljevic, M. B. Whitwick, A. Kis, Integrated circuits and logic operations based on single-layer MoS_2. *ACS Nano* **5**, 9934–9938 (2011).
5. E. Liu, Y. Fu, Y. Wang, Y. Feng, H. Liu, X. Wan, W. Zhou, B. Wang, L. Shao, C.-H. Ho, Y.-S. Huang, Z. Cao, L. Wang, A. Li, J. Zeng, F. Song, X. Wang, Y. Shi, H. Yuan, H. Y. Hwang, Y. Cui, F. Miao, D. Xing, Integrated digital inverters based on two-dimensional anisotropic ReS_2 field-effect transistors. *Nat. Commun.* **6**, 6991 (2015).
6. Q. H. Wang, K. Kalantar-Zadeh, A. Kis, J. N. Coleman, M. S. Strano, Electronics and optoelectronics of two-dimensional transition metal dichalcogenides. *Nat. Nanotechnol.* **7**, 699–712 (2012).
7. E. Liu, M. Long, J. Zeng, W. Luo, Y. Wang, Y. Pan, W. Zhou, B. Wang, W. Hu, Z. Ni, Y. You, X. Zhang, S. Qin, Y. Shi, K. Watanabe, T. Taniguchi, H. Yuan, H. Y. Hwang, Y. Cui, F. Miao, D. Xing, High responsivity phototransistors based on few-layer ReS_2 for weak signal detection. *Adv. Funct. Mater.* **26**, 1938–1944 (2016).
8. O. Lopez-Sanchez, D. Lembke, M. Kayci, A. Radenovic, A. Kis, Ultrasensitive photodetectors based on monolayer MoS_2. *Nat. Nanotechnol.* **8**, 497–501 (2013).
9. M. Chhowalla, H. S. Shin, G. Eda, L.-J. Li, K. P. Loh, H. Zhang, The chemistry of two-dimensional layered transition metal dichalcogenide nanosheets. *Nat. Chem.* **5**, 263–275 (2013).
10. D. Sarkar, X. Xie, W. Liu, W. Cao, J. Kang, Y. Gong, S. Kraemer, P. M. Ajayan, K. Banerjee, A subthermionic tunnel field-effect transistor with an atomically thin channel. *Nature* **526**, 91–95 (2015).
11. C. Gong, H. Zhang, W. Wang, L. Colombo, R. M. Wallace, K. Cho, Band alignment of two-dimensional transition metal dichalcogenides: Application in tunnel field effect transistors. *Appl. Phys. Lett.* **103**, 053513 (2013).
12. C.-H. Lee, G.-H. Lee, A. M. van der Zande, W. Chen, Y. Li, M. Han, X. Cui, G. Arefe, C. Nuckolls, T. F. Heinz, J. Guo, J. Hone, P. Kim, Atomically thin p-n junctions with van der Waals heterointerfaces. *Nat. Nanotechnol.* **9**, 676–681 (2014).
13. D. Li, M. Chen, Z. Sun, P. Yu, Z. Liu, P. M. Ajayan, Z. Zhang, Two-dimensional non-volatile programmable p-n junctions. *Nat. Nanotechnol.* **12**, 901–906 (2017).
14. M. M. Furchi, A. Pospischil, F. Libisch, J. Burgdörfer, T. Mueller, Photovoltaic effect in an electrically tunable van der Waals heterojunction. *Nano Lett.* **14**, 4785–4791 (2014).
15. Y. Deng, Z. Luo, N. J. Conrad, H. Liu, Y. Gong, S. Najmaei, P. M. Ajayan, J. Lou, X. Xu, P. D. Ye, Black phosphorus-monolayer MoS_2 van der Waals heterojunction p–n diode. *ACS Nano* **8**, 8292–8299 (2014).
16. C. Gong, L. Colombo, R. M. Wallace, K. Cho, The unusual mechanism of partial fermi level pinning at metal–MoS_2 interfaces. *Nano Lett.* **14**, 1714–1720 (2014).
17. X. Liu, D. Qu, J. Ryu, F. Ahmed, Z. Yang, D. Lee, W. J. Yoo, P-type polar transition of chemically doped multilayer MoS_2 transistor. *Adv. Mater.* **28**, 2345–2351 (2016).
18. S. Das, A. Prakash, R. Salazar, J. Appenzeller, Toward low-power electronics: Tunneling phenomena in transition metal dichalcogenides. *ACS Nano* **8**, 1681–1689 (2014).
19. S. Das, J. Appenzeller, WSe_2 field effect transistors with enhanced ambipolar characteristics. *Appl. Phys. Lett.* **103**, 103501 (2013).
20. D. H. Keum, S. Cho, J. H. Kim, D.-H. Choe, H.-J. Sung, M. Kan, H. Kang, J.-Y. Hwang, S. W. Kim, H. Yang, K. J. Chang, Y. H. Lee, Bandgap opening in few-layered monoclinic $MoTe_2$. *Nat. Phys.* **11**, 482–486 (2015).
21. I. G. Lezama, A. Arora, A. Ubaldini, C. Barreteau, E. Giannini, M. Potemski, A. F. Morpurgo, Indirect-to-direct band gap crossover in few-layer $MoTe_2$. *Nano Lett.* **15**, 2336–2342 (2015).
22. C. Ruppert, O. B. Aslan, T. F. Heinz, Optical properties and band gap of single- and few-layer $MoTe_2$ crystals. *Nano Lett.* **14**, 6231–6236 (2014).
23. S. Cho, S. Kim, J. H. Kim, J. Zhao, J. Seok, D. H. Keum, J. Baik, D.-H. Choe, K. J. Chang, K. Suenaga, S. W. Kim, Y. H. Lee, H. Yang, Phase patterning for ohmic homojunction contact in $MoTe_2$. *Science* **349**, 625–628 (2015).
24. Y. Qi, P. G. Naumov, M. N. Ali, C. R. Rajamathi, W. Schnelle, O. Barkalov, M. Hanfland, S.-C. Wu, C. Shekhar, Y. Sun, V. Süß, M. Schmidt, U. Schwarz, E. Pippel, P. Werner, R. Hillebrand, T. Förster, E. Kampert, S. Parkin, R. J. Cava, C. Felser, B. Yan, S. A. Medvedev, Superconductivity in Weyl semimetal candidate $MoTe_2$. *Nat. Commun.* **7**, 11038 (2016).
25. Y.-F. Lin, Y. Xu, S.-T. Wang, S.-L. Li, M. Yamamoto, A. Aparecido-Ferreira, W. Li, H. Sun, S. Nakaharai, W.-B. Jian, K. Ueno, K. Tsukagoshi, Ambipolar $MoTe_2$ transistors and their applications in logic circuits. *Adv. Mater.* **26**, 3263–3269 (2014).
26. K. Zhang, X. Fang, Y. Wang, Y. Wan, Q. Song, W. Zhai, Y. Li, G. Ran, Y. Ye, L. Dai, Ultrasensitive near-infrared photodetectors based on a graphene-$MoTe_2$-graphene vertical van der Waals heterostructure. *ACS Appl. Mater. Interfaces* **9**, 5392–5398 (2017).
27. C. Kim, I. Moon, D. Lee, M. S. Choi, F. Ahmed, S. Nam, Y. Cho, H.-J. Shin, S. Park, W. J. Yoo, Fermi level pinning at electrical metal contacts of monolayer molybdenum dichalcogenides. *ACS Nano* **11**, 1588–1596 (2017).
28. S. Nakaharai, M. Yamamoto, K. Ueno, Y.-F. Lin, S.-L. Li, K. Tsukagoshi, Electrostatically reversible polarity of ambipolar α-$MoTe_2$ transistors. *ACS Nano* **9**, 5976–5983 (2015).
29. S. Larentis, B. Fallahazad, H. C. P. Movva, K. Kim, A. Rai, T. Taniguchi, K. Watanabe, S. K. Banerjee, E. Tutuc, Reconfigurable complementary monolayer $MoTe_2$ field-effect transistors for integrated circuits. *ACS Nano* **11**, 4832–4839 (2017).

30. W. Luo, M. Zhu, G. Peng, X. Zheng, F. Miao, S. Bai, X.-A. Zhang, S. Qin, Carrier modulation of ambipolar few-layer $MoTe_2$ transistors by MgO surface charge transfer doping. *Adv. Funct. Mater.* **28**, 1704539 (2017).
31. D. Qu, X. Liu, M. Huang, C. Lee, F. Ahmed, H. Kim, R. S. Ruoff, J. Hone, W. J. Yoo, Carrier-type modulation and mobility improvement of thin $MoTe_2$. *Adv. Mater.* **29**, 1606433 (2017).
32. J. Chen, Z. Feng, S. Fan, S. Shi, Y. Yue, W. Shen, Y. Xie, E. Wu, C. Sun, J. Liu, H. Zhang, W. Pang, D. Sun, W. Feng, Y. Feng, S. Wu, D. Zhang, Contact engineering of molybdenum ditelluride field effect transistors through rapid thermal annealing. *ACS Appl. Mater. Interfaces* **9**, 30107–30114 (2017).
33. A. Pezeshki, S. H. Hosseini Shokouh, P. J. Jeon, I. Shackery, J. S. Kim, I.-K. Oh, S. C. Jun, H. Kim, S. Im, Static and dynamic performance of complementary inverters based on nanosheet α-$MoTe_2$ *p*-channel and MoS_2 *n*-channel transistors. *ACS Nano* **10**, 1118–1125 (2016).
34. L. Ju, J. Velasco Jr., E. Huang, S. Kahn, C. Nosiglia, H.-Z. Tsai, W. Yang, T. Taniguchi, K. Watanabe, Y. Zhang, G. Zhang, M. Crommie, A. Zettl, F. Wang, Photoinduced doping in heterostructures of graphene and boron nitride. *Nat. Nanotechnol.* **9**, 348–352 (2014).
35. J. D. Yao, Z. Q. Zheng, J. M. Shao, G. W. Yang, Stable, highly-responsive and broadband photodetection based on large-area multilayered WS_2 films grown by pulsed-laser deposition. *Nanoscale* **7**, 14974–14981 (2015).
36. G.-H. Lee, Y.-J. Yu, X. Cui, N. Petrone, C.-H. Lee, M. S. Choi, D.-Y. Lee, C. Lee, W. J. Yoo, K. Watanabe, T. Taniguchi, C. Nuckolls, P. Kim, J. Hone, Flexible and transparent MoS_2 field-effect transistors on hexagonal boron nitride-graphene heterostructures. *ACS Nano* **7**, 7931–7936 (2013).
37. D. Akinwande, N. Petrone, J. Hone, Two-dimensional flexible nanoelectronics. *Nat. Commun.* **5**, 5678 (2014).
38. A. Di Bartolomeo, L. Genovese, F. Giubileo, L. Iemmo, G. Luongo, T. Foller, M. Schleberger, Hysteresis in the transfer characteristics of MoS_2 transistors. *2D Mater.* **5**, 015014 (2018).
39. D. Jariwala, V. K. Sangwan, C.-C. Wu, P. L. Prabhumirashi, M. L. Geier, T. J. Marks, L. J. Lauhon, M. C. Hersam, Gate-tunable carbon nanotube-MoS_2 heterojunction p-n diode. *Proc. Natl. Acad. Sci. U.S.A.* **110**, 18076–18080 (2013).
40. A. Nourbakhsh, A. Zubair, M. S. Dresselhaus, T. Palacios, Transport properties of a MoS_2/WSe_2 heterojunction transistor and its potential for application. *Nano Lett.* **16**, 1359–1366 (2016).
41. A. Pospischil, M. M. Furchi, T. Mueller, Solar-energy conversion and light emission in an atomic monolayer p-n diode. *Nat. Nanotechnol.* **9**, 257–261 (2014).
42. B. W. H. Baugher, H. O. H. Churchill, Y. Yang, P. Jarillo-Herrero, Optoelectronic devices based on electrically tunable p-n diodes in a monolayer dichalcogenide. *Nat. Nanotechnol.* **9**, 262–267 (2014).
43. F. Wang, L. Yin, Z. X. Wang, K. Xu, F. M. Wang, T. A. Shifa, Y. Huang, C. Jiang, J. He, Configuration-dependent electrically tunable van der Waals heterostructures based on $MoTe_2$/MoS_2. *Adv. Funct. Mater.* **26**, 5499–5506 (2016).
44. Y. Liu, Y. Cai, G. Zhang, Y.-W. Zhang, K.-W. Ang, Al-doped black phosphorus p–n homojunction diode for high performance photovoltaic. *Adv. Funct. Mater.* **27**, 1604638 (2017).
45. Z. Wang, F. Wang, L. Yin, Y. Huang, K. Xu, F. Wang, X. Zhan, J. He, Electrostatically tunable lateral $MoTe_2$ p-n junction for use in high-performance optoelectronics. *Nanoscale* **8**, 13245–13250 (2016).
46. N. Huo, G. Konstantatos, Ultrasensitive all-2D MoS_2 phototransistors enabled by an out-of-plane MoS_2 PN homojunction. *Nat. Commun.* **8**, 572 (2017).

Acknowledgments

Funding: This work was supported by the National Science Foundation of China (no. 21405109) and the Seed Foundation of State Key Laboratory of Precision Measurement Technology and Instruments, China (no. Pilt1710). **Author contributions:** E.W., Y.X., D.Z., J.L., and C.Z. conceived and designed the experiments. E.W. investigated the doping phenomenon and doping mechanisms and measured relevant electrical transport of the $MoTe_2$ transistor. Y.X. and X.H. fabricated the homogeneous $MoTe_2$ p-n junction and investigated its optoelectronic properties. J.Z. and H.Z. performed SEM, Raman, and AFM measurement. E.W., J.L., and D.Z. were mainly responsible for preparing the manuscript with input from all other authors. All authors discussed the results and commented on the manuscript. The manuscript was written through contributions of all authors. All authors have given approval to the final version of the manuscript. **Competing interests:** The authors declare that they have no competing interests. **Data and materials availability:** All data needed to evaluate the conclusions in the paper are present in the paper and/or the Supplementary Materials. Additional data related to this paper may be requested from the authors.

Submitted 14 September 2018
Accepted 21 March 2019
Published 3 May 2019
10.1126/sciadv.aav3430

Citation: E. Wu, Y. Xie, J. Zhang, H. Zhang, X. Hu, J. Liu, C. Zhou, D. Zhang, Dynamically controllable polarity modulation of $MoTe_2$ field-effect transistors through ultraviolet light and electrostatic activation. *Sci. Adv.* **5**, eaav3430 (2019).